Journal of Applied Fluid Mechanics, Vol. 16, No. 10, pp. 1974-1988, 2023.
Available online at www.jafmonline.net, ISSN 1735-3572, EISSN 1735-3645.
https://doi.org/10.47176/jafm.16.10.1855

Determination of Optimum Parameter Space of a Fluidic Thrust Vectoring System based on Coanda Effect Using Gradient-Based Optimization Technique

E. Kara[1†] and D. F. Kurtuluş[2]

[1] *Gaziantep University, Aerospace Engineering Department, Gaziantep, 27310, Turkey*
[2] *METU, Aerospace Engineering Department, Ankara, 06800, Turkey*

†*Corresponding Author Email: emrekara@gantep.edu.tr*

ABSTRACT

In the realm of aviation, jet propulsion systems serve to provide enhanced maneuverability and to make sure that the aircraft thrust is accurately and precisely regulated during take-off and landing operations. The movement of aerodynamic control surfaces (flaps, slats, elevators, ailerons, spoilers, wing attachments) determines the mobility of practically all aircraft types. Recognized as dependable components in the aviation world for take-off and landing tasks, these control surfaces are being replaced by fluidic thrust vectoring (FTV) systems, especially in small unmanned aerial vehicles (UAVs) and short or vertical take-off and landing aircraft. The FTV system is capable of directing thrust in any preferred direction without the need for any movable components. This paper numerically examines the FTV system by utilizing computational fluid dynamics (CFD) and an optimization technique based on gradients of the system components to understand the physics of the Coanda effect in FTV systems. This research employs gradient-based optimization for nozzle design in order to optimize the parameter space for different velocity ratios (VR) by calculating the moment around the upper Coanda surface, which is used to represent the jet deflection angle. In that context, four different Coanda surface-pintle pair designs for four different VRs are produced. The parameter space shows significant improvement in all four configurations, and results reveal that all output parameters successfully delay separation on the thrust vectoring system's upper Coanda surface. Finally, four optimum design suggestions are tested at various VRs, and the most efficient and proper design is recommended based on output parameters.

Article History

Received March 4, 2023
Revised May 24, 2023
Accepted May 27, 2023
Available online July 29, 2023

Keywords:

Coanda effect
Fluidic thrust vectoring
Gradient-based optimization
Jet deflection
Thrust vectoring efficiency

1. INTRODUCTION

Co-flow fluidic thrust vectoring (FTV) systems have been widely used for the last decade in aerospace applications (Subhash & Dumas, 2013; Trancossi et al., 2014; Banazadeh & Saghafi, 2017; Warsop et al., 2019). The aeronautical industry at the current state-of-the-art utilizes heavy and expensive mechanical FTV systems, whereas FTV concepts employing the Coanda effect have the benefits of being lightweight and agile without any moving components. The mechanical FTV systems of the current aeronautical industry have components that are movable, but hefty and costly. FTV ideas exploiting the Coanda effect can be a substitute for mechanical ones with the advantages of being lightweight and agile without movable components.

FTV systems provide the rotation of thrust effectively in any desired direction without movable components using the Coanda effect over the outlet surface. The system mainly draws air through two inlet ducts with electric motors at different speeds. Consequently, the flow direction is deflected by creating pressure difference due to the different speeds of air-jets passing over two Coanda surfaces.

The Coanda effect is principally changing the flow direction towards the slope of the surface owing to the adhesion force exerted on the surface by the fluid itself when a high-speed fluidic jet passes over a convex surface. The Coanda effect is not only employed for aeronautics

NOMENCLATURE

A	cross-sectional area	T	total thrust
C_f	skin-friction coefficient	T_n	normal thrust
$\bar{c}$	input parameter	T_{ref}	reference thrust
F_s	safety factor	T_x	thrust in the axial direction
h	vertical location of center of the Coanda surface curvature	T_y	thrust in the transverse direction
J	observable	u	face-averaged velocity
L	Lagrangian	u_{ref}	reference velocity
M	simplified system Jacobian	u_{tot}	combined velocity
$\vec{M}_A$	moment around upper Coanda surface	u_1	variable velocity in inlet-1
$\dot{m}$	mass flow rate	u_2	constant velocity in inlet-2
P	static pressure (gage)	y_s	vertical location of separation point
PP	performance parameter	y^+	non dimensional length scale
q	order of accuracy	α	under-relaxation factor
$\bar{q}$	flow solution	η	thrust vectoring efficiency
$\tilde{q}$	vector of Lagrange multipliers	θ	jet angle
R	residual	θ_s	jet deflection (separation) angle
r	refinement ratio	θ_T	thrust vectoring angle
r_c	radius of the Coanda surface curvature	ρ_{ref}	reference density
$\vec{r}$	vector from the specified moment center	τ_w	wall shear stress

applications (Jain et al., 2015) but also in heating/cooling systems (Sidiropoulos & Vlachopoulos, 2000) and marine applications (El Halal et al., 2019). Mainly, FTV designs using Coanda effect comprise systems such as Newman (1961) system, Juvet (1994) system, or High Speed Orienting Momentum with Enhanced Reversibility (HOMER) system (Trancossi et al., 2011). Newman system uses a single jet of air that is guided over a convex surface (Trancossi et al., 2016a), which is the ancestor of fluid propulsion guidance systems (Fig. 1a). Juvet (1994) system uses two main air jets and a control air jet that are directed over convex surfaces (Fig. 1b). HOMER system (Fig. 1c) which is developed by Trancossi et al. (2011) guides a main jet and a control jet between two Coanda surfaces. The nozzle geometry, which can operate at subsonic speeds, was developed in a European Union project called ACHEON (Trancossi & Dumas, 2011; ACHEON, 2015; Trancossi et al., 2016a). An extensive presentation of the mathematical models of the above three systems can be found in Trancossi et al. (2016b).

Among the three aforementioned designs, the current study focuses on the HOMER nozzle system to investigate its adaptation to VTOL, STOL, and UAV systems. The HOMER nozzle system belongs to the co-flow Coanda category of FTV systems. As seen in Fig. 1c, the juxtaposition of an electric motor providing a variable velocity, u_1 in inlet-1, and another electric motor providing a constant velocity, u_2 in inlet-2 allows the air jets to travel in parallel, converge as they pass over converging-diverging Coanda surfaces, and twist out of the nozzle in the direction of jet angle, θ, with combined velocity u_{tot}. Therefore, the ratio of the variable velocity to the constant velocity becomes a function of the thrust vectoring angle control.

As a consequence of a comprehensive review of previous studies (Springer, 2008; Trancossi et al., 2011; Subhash & Dumas, 2013; Trancossi et al., 2014;

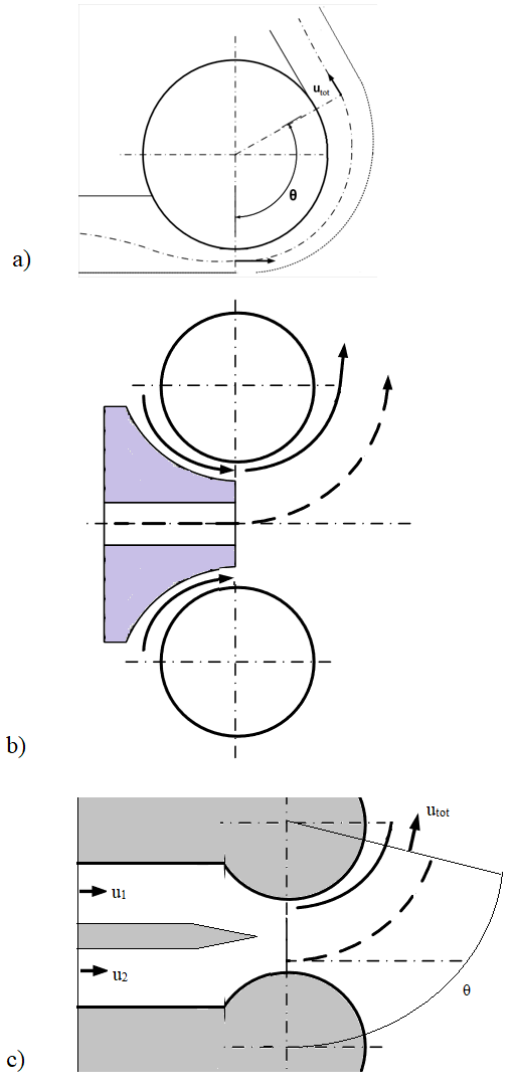

Fig. 1 (a) Newman system, (b) Juvet system and (c) HOMER nozzle system. All modified from Trancossi et al. (2016b)

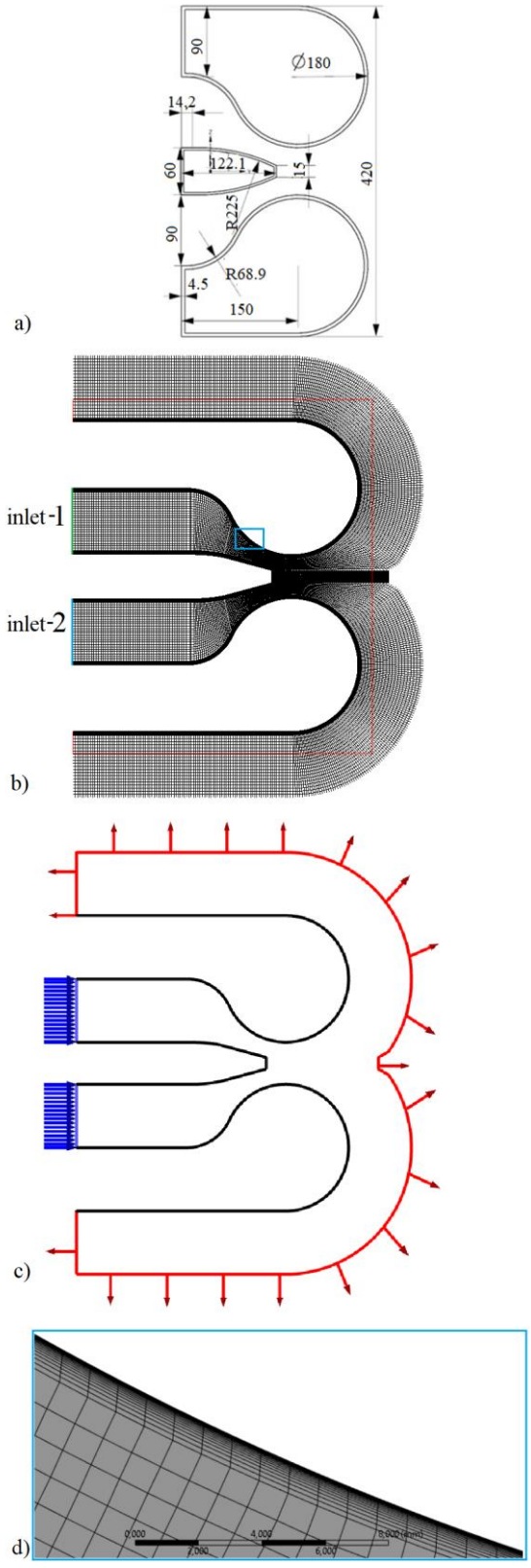

Fig. 2 (a) Dimensions of the FTV system (in mm), (b) computational domain, (c) mesh structure with inlet boundary conditions, other boundary conditions (no-slip and outlet), (d) close look to the inflation layers in the blue box of (b)

Cen et al., 2015; Trancossi et al., 2016b; Panneer & Thiyagu, 2020, Kara and Erpulat, 2021), the HOMER nozzle design calculations for different velocity ratios (VR = u_1/u_2) can be interpreted in three main groups: thrust-related parameter calculations, the maximum jet deflection (separation) angle investigations, and the optimization of the nozzle (Coanda-pintle pair) design. In all these studies, it is observed as a gap that a wide range of VR values is not considered, and their effects on the output parameters are not examined.

In this study, gradient-based optimization is used to optimize the parameter space for different VRs using the moment around the upper Coanda surface, representing the jet deflection angle, θ_s, as the observable parameter in the gradient-based optimization module of Ansys Fluent. Furthermore, the FTV systems are analyzed in terms of thrust vectoring efficiency (Yahaghi, 2011; Jain et al., 2015), which is also mentioned by Das et al. (2016) as the efficiency parameter for co-flow FTV systems using Coanda surfaces. The original and the optimized systems are compared in terms of their efficiency and performance parameter (PP) values suggested by Trancossi et al. (2014).

This research attempts to give a precise definition of the output parameters and the mathematical modeling applicable to the optimized system. The maximum jet deflection angle is attained for different VRs.

2. MATERIALS AND METHODS

FTV system using the Coanda effect is developed using mathematical modeling, numerical simulations, and optimization using a gradient-based optimization technique.

2.1 Mathematical Modeling

The dimensions of the proposed FTV system are shown in Fig. 2a, which is based on the HOMER nozzle system (Trancossi et al., 2016b) with minor changes for improved performance. In contrast to the original design, the current FTV system (Fig. 2) has a more unified joint of the converging-diverging section to the Coanda surface to secure an aerodynamic flow and also has a blunt pintle nose to be used as an optimization measure to avoid having highly skewed elements during the grid formation procedure of optimized shapes.

The computational domain of the study is given in Fig. 2b, while Eqs. (1) to (6) are generated for the control volume surrounded by a red boundary in the mesh structure as shown in Fig. 2b, where the inlet sections are highlighted in green and blue for inlet-1 and inlet-2, respectively. In Fig. 2c the walls are highlighted in black, and the outlet boundaries in red. The mesh structure is based on the 2D quadrilateral unstructured grids (Fig. 2b) and quadrilateral elements are generated for the inflation layers (Fig. 2d) near the walls.

In this study, the velocity inlet boundary condition at inlet-1 is taken as constant at u_1 = 10 m/s, and the velocity inlet boundary condition at inlet-2 is varied between 15 and 45 m/s (Fig. 2c). The no-slip boundary condition is defined at the walls, i.e. the upper Coanda surface, the lower Coanda surface and the pintle (Fig. 2c). The type of boundary condition at the outlet is the pressure

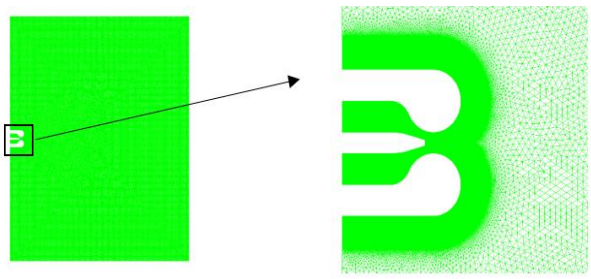

Fig. 3 Larger domain selection and the close-up view of the mesh to consider the physical limits of the computational problem

Table 1 Comparisons of original domain and larger domain results on the output parameters

Parameter	Original	Larger	Difference (%)
$\lvert\vec{M_A}\rvert$	0.512	0.510	0.5
T(N)	25.689	26.095	-1.6
η (%)	31.043	31.532	-1.6
T_y (N)	25.668	26.072	-1.6
T_x (N)	-1.043	-1.104	-0.6
PP	91.128	90.883	+0.3
θ_T (°)	69.226	69.040	+0.3

outlet and set to atmospheric pressure, considering that the flow is in contact with the atmosphere at the outlet.

The effect of the computational domain size was also investigated to observe the farfield dependency of the numerical results. Fluid domain is increased ten times than the original size in both x and y directions and the results are compared or VR = 3.0 as shown in Fig. 3. It is observed that the error was less than 1.6% (Table 1) in terms of the output parameters investigated.

In addition, the comparison of the velocity contour of both domains shows similar jet deflection angles as shown in Fig. 4.

In an FTV system, the most decisive parameter to be analyzed correctly is the total thrust, T, and its components, since all other output parameters (thrust vectoring efficiency, η, thrust vectoring angle, θ_T, jet deflection angle, θ_s, and performance parameter, PP) depend on the components of the thrust.

The axial thrust, T_x, and transverse thrust, T_y are derived from the x-momentum equation and y-momentum equation, respectively, and presented in Eq. (1) and Eq. (2):

$$T_x = \dot{m}_3 u_{3,x} - \dot{m}_2 u_2 - \dot{m}_1 u_1 + P_3 A_3 - P_2 A_2 - P_1 A_1 \quad (1)$$

$$T_y = \dot{m}_3\, u_{3,y} \quad (2)$$

where $\dot{m}$ is the mass flow rate, u is the face-averaged velocity, P is the static (gage) pressure relative to atmospheric pressure, A is the cross-sectional area and subscripts x and y represent axial and transverse directions, respectively. In addition, subscripts 1, 2, and 3 describe inlet-1, inlet-2, and outlet sections, respectively.

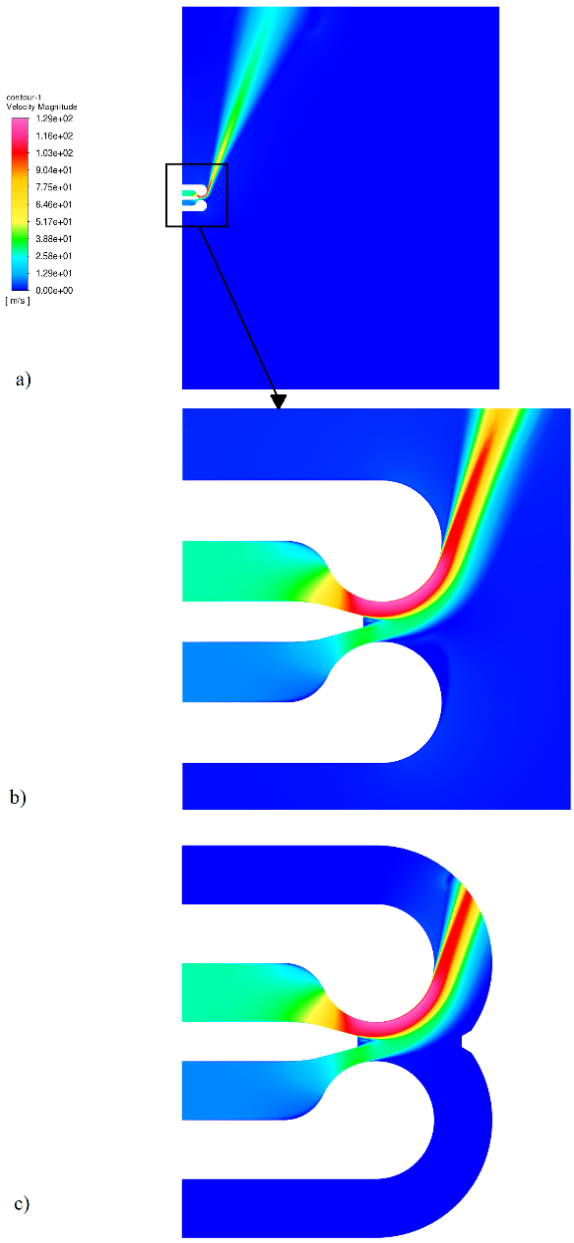

Fig. 4 Velocity contours a) 10 times larger farfield domain, b) close-up view to the larger domain, c) original farfield domain

Eq. (3) and Eq. (4) show the thrust vectoring efficiency, η, and thrust vectoring angle, θ_T (Das et al., 2016), respectively:

$$\eta = \frac{T_y}{T_{ref}} \times 100(\%) \quad (3)$$

$$\theta_T = \tan^{-1}\left|\frac{T_y}{T_x}\right| \quad (4)$$

where T_{ref} is the reference thrust, which is the maximum thrust achieved with FTV system. The performance parameter (PP) (Trancossi et al., 2014) represents the aerodynamic performance characteristic of an FTV system (Eq. (5)).

$$PP = \theta_T / \left(\frac{m_1}{m_1+m_2}\right) \quad (5)$$

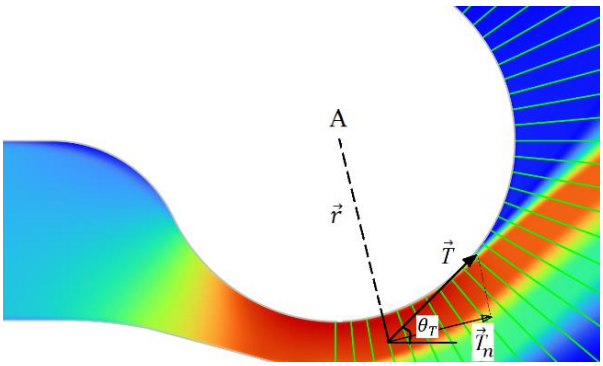

Fig. 5 Moment about the specified moment center, point A and CFD exemplification of the moment calculation

where m_1 and m_2 stand for the mass flow rates at the inlet-1 and inlet-2, respectively.

In this study, PP is chosen as one of the main efficiency parameters, in addition to η. All the above output parameters are optimized in the Results section for different VRs (1.5 – 2.0 – 3.0 – 4.5) using the moment, $\vec{M}$, representing the jet deflection angle, θ_s, as the observable parameter in the gradient-based optimization module of Ansys Fluent. The moment around the upper Coanda surface, $\vec{M}_A$, is defined as:

$$\vec{M}_A = \vec{r} \times \vec{T}_n \tag{6}$$

where $\vec{r}$ is the vector from the specified moment center (point A) to the force origin and $\vec{T}_n$ is the specified thrust vector perpendicular to $\vec{r}$ as given in Fig. 5.

The moment calculation is exemplified by the velocity contours in Fig. 5, where the normal component of $\vec{T}$, represented by $\vec{T}_n$, follows the flow direction and $\vec{r}$ intersects the line of action, i.e. the total thrust ($\vec{T}$) direction.

2.2 Mesh Independence Study

The first step before proceeding to the CFD solution of the relevant FTV system is to conduct a mesh independence study. In 1994, Roache (1994) developed a method called "Grid Convergence Index" (GCI) which was successfully adapted to thrust vectoring systems by Wu et al. (2020). In the mesh independence analysis of the present study, the axial thrust, T_x, transverse thrust, T_y, thrust vectoring angle, θ_T, thrust vectoring efficiency, η, moment around the upper Coanda surface, $\vec{M}_A$, performance parameter, PP and total thrust, T are compared separately to find the smallest number of mesh elements to attain precise results referred to the GCI approach of Roache (1994). Furthermore, it was ensured that the minimum orthogonal quality was at least 0.2 and the average skewness was at most 0.7 for coarse, medium, and fine meshes. The equations used to find the optimum mesh size are as follows:

$$q = \frac{ln\left(\frac{f_1 - f_2}{f_2 - f_3}\right)}{\ln(r)} \tag{7}$$

$$GCI_{1,2} = \frac{F_s\left|\frac{f_2 - f_1}{f_2}\right|}{r^q - 1} \times 100\% \tag{8}$$

$$GCI_{2,3} = \frac{F_s\left|\frac{f_3 - f_2}{f_3}\right|}{r^q - 1} \times 100\% \tag{9}$$

$$\frac{GCI_{1,2}}{r^q \cdot GCI_{2,3}} \sim 1 \tag{10}$$

where q stands for order of accuracy; f_1, f_2, f_3 are T_x, T_y, θ_T, η, PP, and T for coarse, medium, and fine meshes, respectively; F_s is the safety factor; r is the refinement ratio between the coarse, medium, and fine meshes. The aim of Roache's GCI calculation proposal is given by Eq. (10), i.e. to make the ratio between $GCI_{1,2}$ and the product of r^q and $GCI_{2,3}$ approximately 1 so that the medium mesh can be selected as the optimal choice. The calculations for mesh independence are given in the Results section.

2.3 Indication of Jet Deflection (Separation) Angle

In addition to the parameter space summarized in the "Mathematical Modeling" subsection 2.1, another important parameter to consider for a better FTV system is the maximum jet deflection angle. The jet deflection angle is the angle between the axial direction and the point on the Coanda surface, where the skin-friction coefficient, C_f, is locally minimized, becomes almost zero (the threshold of separation from the surface) then returns to higher values (Subhash & Dumas, 2013). θ_s is the angle between transverse of the flow direction and the location of the minimum value of the gradient of the wall shear stress (τ_w) perpendicular to the Coanda surface, i.e. $\partial\tau_w/\partial|\vec{r}| \approx 0$. It should be noted that the thrust vectoring angle, θ_T (Fig. 5), and the jet deflection angle, θ_s are not identical. The former is the angle between the horizontal direction and the tangent of the total thrust, T, to the separation point, and the latter is the angle between the axial direction and the minimum C_f location. Therefore, the separation angle, θ_s, can be achieved in three steps in CFD calculations:

The first step is to position all the points on the Coanda surface in terms of angles using the following transformation:

$$\theta_s = \cos^{-1}\left[\frac{(h - y_s)}{r_c}\right] \tag{11}$$

where h is the vertical location of the center of the Coanda surface curvature, y_s is the vertical location of the separation point on the upper Coanda surface relative to the centerline, and r_c is the radius of the Coanda surface curvature as shown in Fig. 6. The distances h and r_c take constant values of 0.12 m and 0.09 m, respectively.

Second step is to observe C_f (Eq. 12) over the Coanda surface:

$$C_f = \tau_w / \left(\frac{1}{2}\,\rho_{ref}\,{u_{ref}}^2\right) \tag{12}$$

where ρ_{ref} is the reference density and u_{ref} is the reference velocity. In this study, ρ_{ref} is taken as 1.225 kg/m^3 and u_{ref} as the varying inlet velocity for each case; i.e. 15 m/s, 20 m/s, 30 m/s and 45 m/s, for Design-1, Design-2, Design-3 and Design-4, respectively.

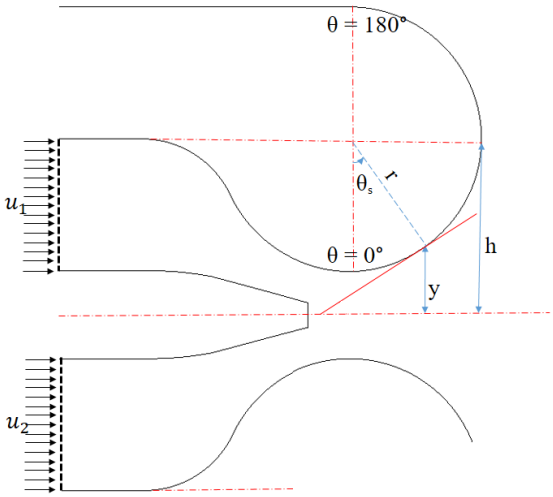

Fig. 6 Indication of the jet deflection angle, θ_s, using the vertical location of the upper Coanda surface

The last step is to find the jet deflection angle when C_f in the first layer mesh is almost zero (which depends on the mesh size). Since the maximum y^+ in the current study is 0.82 (< 1), the procedure for calculating the jet deflection angle is guaranteed to be accurate.

2.4 Gradient-based Optimization

The gradient-based solver is a tool for shape optimization, which estimates the effect of local geometry changes on a target quantity. By using the adjoint solver available in ANSYS (2022), it is possible to calculate the linear derivatives of a single output variable relative to input variable(s). The adjoint workflow is established by computing the gradient, or the speed of alteration of the chosen scalar field, then accumulating the sensitivity data and returning the mapping of the data through the derivatives, followed by adjusting the mesh or surfaces of the computational domain. This procedure is repeatedly implemented, manually and/or automatically, until the most desirable outcome for the design is attained. The following paragraphs describe the working principle and components of gradient-based optimization with the adjoint solver (ANSYS, 2022).

The observable $J(\bar{q}(\bar{c}); \bar{c})$, is calculated for residuals of Navier-Stokes equations and compared with the previous solution. Residuals for continuity, momentum, energy, and turbulence model are required to ensure $J(\bar{q}(\bar{c}); \bar{c}) = 0$ in the machine zero limits, where R stands for residual, $\bar{c}$ is the input parameter, and $\bar{q}$ is the flow solution, such as pressure, velocity. The observable (J) is the scalar quantity of interest (lift, drag, pressure drop, thrust, moment) of the simulation that is checked by the adjoint solver at the end of every workflow for its influence on $\bar{c}$ inputs. The relation between J and $\bar{c}$'s can be formulated using two different methods: The direct method and the adjoint (gradient-based) method (ANSYS, 2022). In this study, the adjoint (gradient-based) method is employed.

Defining the Lagrangian L with the vector of Lagrange multipliers, $\tilde{q}$:

$$L(\bar{q}(\bar{c}), \bar{c}, \tilde{\bar{q}}) = J + \tilde{\bar{q}}^T R \tag{13}$$

Since $R = 0$ at the end of solution, $\tilde{q}$ can be chosen arbitrarily, so it is chosen to be zero:

$$L(\bar{q}(\bar{c}), \bar{c}, \tilde{\bar{q}}) = J \tag{14}$$

The calculation of the gradient of an observable J with respect to an input $\bar{c}$ can be as follows:

$$\frac{dJ}{d\bar{c}} = \frac{dL}{d\bar{c}} = \frac{\partial J}{\partial \bar{q}}\frac{d\bar{q}}{d\bar{c}} + \frac{\partial J}{\partial \bar{c}} + \tilde{\bar{q}}^T\left[\frac{\partial R}{\partial \bar{q}}\frac{d\bar{q}}{d\bar{c}} + \frac{\partial R}{\partial \bar{c}}\right] + \left[\frac{d\tilde{\bar{q}}^T}{d\bar{c}}\right] R \tag{15}$$

where $R = 0$ at the end of the solution. Rearranging Eq. (15):

$$\frac{dJ}{d\bar{c}} = \frac{d\bar{q}}{d\bar{c}}\left(\frac{\partial J}{\partial \bar{q}} + \tilde{\bar{q}}^T\frac{\partial R}{\partial \bar{q}}\right) + \frac{\partial J}{\partial \bar{c}} + \tilde{\bar{q}}^T\frac{\partial R}{\partial \bar{c}} \tag{16}$$

Choose $\tilde{\bar{q}}^T$ such that the term in parentheses on the right hand side of Eq. (16) is equal to zero, i.e. the following equation is satisfied:

$$\left[\frac{\partial R}{\partial \bar{q}}\right]^T \tilde{\bar{q}} = -\left[\frac{\partial J}{\partial \bar{q}}\right]^T \tag{17}$$

Finally, Eq. (17) reduces to a single linear problem:

$$\frac{dJ}{d\bar{c}} = \frac{\partial J}{\partial \bar{c}} + \tilde{\bar{q}}^T\frac{\partial R}{\partial \bar{c}} \tag{18}$$

Using Eq. (18) in large-scale optimization, the derivative (sensitivity) is calculated, where $\tilde{q}$ is the solution of Eq. (17). This is called the adjoint problem (ANSYS, 2022). Adjoint solves one additional equation for the quantity of interest, i.e. observable. The adjoint (Gradient-based) solver process is executed as shown in the flowchart (Fig. 7) and Eqs. (19) to (21).

$$R = \frac{\partial J}{\partial q_j} - \frac{\partial R_i}{\partial q_j}\tilde{q}_i \tag{19}$$

$$M\Delta\tilde{q}_i = \frac{\partial J}{\partial q_j} - \frac{\partial R_i}{\partial q_j}\tilde{q}_i \tag{20}$$

$$\tilde{q}_i + \alpha_i\Delta\tilde{q}_i \rightarrow \tilde{q}_i \tag{21}$$

where M is the simplified system Jacobian and α is a user-specified under-relaxation factor. The main limitation of the gradient-based optimization process is that it can be applied to an incompressible, ideal gas for laminar, turbulent (currently only k-epsilon, k-omega and GEKO models are integrated into gradient-based optimization in ANSYS Fluent) flows, steady state, moving reference frame, conjugate heat transfer problems (ANSYS, 2022). Frozen turbulence assumption is used except for GEKO.

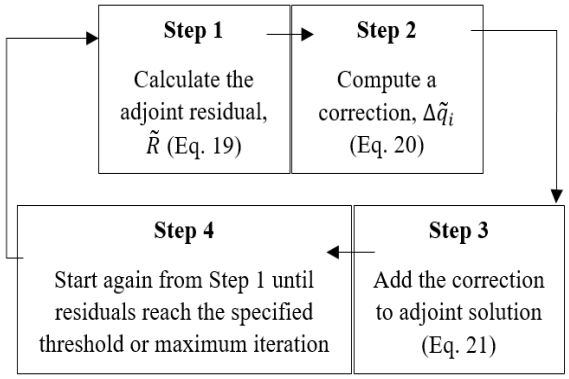

Fig. 7 Flowchart of adjoint (Gradient-based) solver process

Table 2 Mesh independence test results of output parameters

VR	Mesh size	$\lvert\vec{M}_A\rvert$ (N.m)	PP	θ_T (°)	η (%)	T (N)	T_y (N)	T_x (N)	θ_S (°)
1.5	53121	0.039	53.52	32.20	5.73	6.385	4.710	4.312	41.00
	212040	0.025	35.14	21.15	3.99	6.334	3.299	5.395	31.00
	831546	0.024	33.76	20.31	3.83	6.330	3.188	5.480	29.33
2.0	53121	0.120	81.67	54.77	13.59	11.494	11.168	2.716	65.00
	212040	0.075	54.32	36.43	10.32	10.829	8.536	6.664	45.50
	831546	0.072	52.06	34.91	9.91	10.786	8.257	6.939	45.00
3.0	53121	0.563	230.48	175.08	27.95	43.777	22.980	-37.261	135.66
	212040	0.314	91.13	69.23	31.04	25.690	25.668	-1.043	80.00
	831546	0.314	91.15	69.23	30.90	25.762	25.741	-1.050	80.33
4.5	53121	1.784	197.78	166.20	13.08	82.204	10.755	-81.497	182.88
	212040	1.713	201.27	169.14	12.44	82.685	10.286	-82.042	182.86
	831546	1.730	213.96	179.79	12.37	83.290	10.303	-82.651	182.86

This study includes some assumptions to make the modeling and analysis process more efficient. The resulting limitations of the study are stated as follows:

1. All CFD applications are generated with the assumption of steady-state, incompressible, ideal gas flow with the continuity, conservation of momentum, and conservation of energy equations to 2nd order accuracy.
2. The GEKO turbulence model is used to solve and close the Navier-Stokes equations. GEKO is a two-equation model based on the k-omega model formulation with the additional flexibility to be tuned in a wide range of flow conditions.
3. A mesh independence test is performed to determine the optimal mesh for the study. For the final mesh, the first layer height is chosen to be 5×10^{-6} m to meet the criterion of $y^+ < 1$ at boundaries.

3. RESULTS

The adjoint solver process is employed to the Coanda surface and pintle geometries of the thrust vectoring assembly such that the moment around the upper Coanda surface is chosen as the observable value to delay separation from the surface.

3.1 Mesh Independence Study Results

Three different mesh sizes are tested for each VR (Table 2). All meshes are created by inflating 20 layers from solid surfaces with a growth rate of 1.2, where the first layer height is 5×10^{-6} m using the first-layer thickness method to meet the criterion $y^+ < 1$. Mesh independence tests are performed for these meshes with F_s = 1.25 (Roache, 1994; Wu et al., 2020) and r = 4. The goal is to have $\frac{GCI_{1,2}}{r^q \cdot GCI_{2,3}} \sim 1$ at the end of the GCI study, as suggested by Roache (1994). Mesh independence test results for each mesh size and VR are provided in Table 2 for all system variables, i.e. moment around the upper Coanda surface, $\vec{M}_A$, performance parameter, PP, thrust vectoring angle, θ_T, thrust vectoring efficiency, η, total thrust, T, thrust in transverse direction, T_y, thrust in axial direction, T_x, and mesh independence study parameters (q, $GCI_{1,2}$, $GCI_{1,3}$, $\frac{GCI_{1,2}}{r^q \cdot GCI_{2,3}}$) for each system variable (output parameter) are given in Table 3.

Roache's mesh independence test is applied for all output parameters using Roache's parameters given in Eqs. (7) to (10) and the medium mesh is selected to offer further analysis for the current study.

The thrust values, T_x and T_y, are expressed for VR values of 1.5, 2.0, 3.0, and 4.5 using the Eqs. (1) and (2), respectively. T is the root sum of the squares of T_x and T_y. Other variables (θ_T, η, PP) are calculated using Eqs. (3) to (6). The dependence of the separation point on the mesh close to the wall is also investigated by observing the separation angle, θ_S, at the upper Coanda surface using Eq. (11). These expressions are generated as output parameters in ANSYS Fluent, all of which are solved to 2nd order accuracy with the continuity, conservation of momentum, and conservation of energy equations for a steady, incompressible, ideal gas flow. In this study, as tabulated in Table 2, T_{ref} values are found to be 82.204 N, 82.685 N, and 83.290 N for coarse, medium, and fine meshes, respectively, for VR = 4.5.

Following the outputs given in Table 3, the mesh independence tests are performed and the results of all dependent output parameters reveal that $\frac{GCI_{1,2}}{r^q \cdot GCI_{2,3}} \sim 1$. In addition to the mesh sensitivity test, a comparison of the skin-friction coefficient, C_f, for each VR is estimated for the upper Coanda surface of the FTV system in Fig. 8. Mesh-2 is almost identical to the Mesh-3, which is 4 times denser, in terms of C_f estimation performance.

Following the mesh sensitivity study and the results presented in Fig. 8, medium mesh (Mesh-2 with element size 212040) is selected as the most appropriate mesh for the CFD study and employed for gradient-based optimization in the next section. After the solutions are completed, y^+ values are also checked for the same mesh size. With 20 nodal points in the boundary layer, a maximum of 0.82 and an average of 0.20 are calculated for y^+. These are acceptable values for gradient-based optimization in the turbulence model of SST k-omega or GEKO since average y^+ should be less than 1 and at least 15 nodal points should be placed inside the boundary layer for near-wall treatment as recommended in the reference (Menter et al., 2019). GEKO turbulence model without non-linear terms (Menter et al., 2019) is chosen since Reynolds stress tensor (the non-linear term) has a negligible effect on the estimation of the skin-friction

Table 3 Mesh independence study parameters for each system variable

VR	Mesh independence study parameters	$\left\|\vec{M}_A\right\|$ (N.m)	PP	θ_T (°)	η (%)	T (N)	T_y (N)	T_x (N)	θ_S (°)
1.5	q	1.948	1.86	1.86	1.71	1.710	1.829	1.842	1.29
	$GCI_{1,2}$	5.399	5.33	5.33	5.64	0.105	4.596	2.119	8.08
	$GCI_{1,3}$	0.378	0.42	0.42	0.55	0.010	0.377	0.162	1.42
	$\frac{GCI_{1,2}}{r^q \cdot GCI_{2,3}}$	0.960	0.96	0.96	0.96	0.999	0.966	1.016	0.95
2.0	q	1.931	1.80	1.80	1.50	1.974	1.621	1.922	2.64
	$GCI_{1,2}$	5.434	5.69	5.70	5.66	0.532	4.557	5.546	1.41
	$GCI_{1,3}$	0.390	0.49	0.49	0.74	0.035	0.498	0.371	0.04
	$\frac{GCI_{1,2}}{r^q \cdot GCI_{2,3}}$	0.960	0.96	0.96	0.96	0.996	0.967	1.041	0.99
3.0	q	5.763	6.22	6.92	2.24	3.978	2.605	6.193	3.67
	$GCI_{1,2}$	0.034	0.03	0.01	0.58	0.356	0.364	0.811	0.52
	$GCI_{1,3}$	1.143E-05	6.13E-06	8.97E-07	0.03	0.001	0.010	1.507E-04	0.01
	$\frac{GCI_{1,2}}{r^q \cdot GCI_{2,3}}$	1.000	1.00	1.00	1.00	1.003	1.003	1.006	1.00
4.5	q	1.039	-0.93	-0.93	1.61	-0.166	2.369	-0.079	0.79
	$GCI_{1,2}$	1.594	-2.99	-3.00	0.78	-3.531	0.222	-8.038	0.01
	$GCI_{1,3}$	0.374	-10.23	-10.22	0.08	-4.415	0.008	-8.898	0.01
	$\frac{GCI_{1,2}}{r^q \cdot GCI_{2,3}}$	1.010	1.06	1.06	0.99	1.007	1.002	1.007	1.00

Table 4 Variation of the output parameters for different VR values

VR	Jet deflection angle, θ_s (°)	$\left\|\vec{M}_A\right\|$ (N.m)	PP	θ_T (°)	η (%)	T (N)	T_y (N)	T_x (N)
1.5	31.00	0.025	35.14	21.15	3.99	6.334	3.299	5.395
2.0	45.50	0.075	54.32	36.43	10.32	10.829	8.536	6.664
3.0	80.00	0.314	91.13	69.23	31.04	25.690	25.668	-1.043
4.5	182.86	1.713	201.27	169.14	12.44	82.685	10.286	-82.042

coefficient and corresponding parameter of jet deflection angle (Menter et al., 2021). In the GEKO turbulence model, the main parameter for tuning separation prediction in jet flow is the separation parameter, C_{sep}. The most accurate solutions for separated flows of round jets are captured with C_{sep} = 1.75 to 2.00, as proven by Menter et al. (2019), with higher values resulting in excessive separation. Therefore, the separation parameter, C_{sep} = 1.75 is chosen in the GEKO turbulence model and other constants are left as default. In the following subsection, the jet deflection angle, which is the backbone of the FTV systems, is analyzed for different VRs.

3.2 Jet Deflection (Separation) Angle Calculations

C_f variation with jet angle (θ) is given in Fig. 9 for VRs = 1.5, 2.0, 3.0, and 4.5. The jet deflection angle, θ_s, is the angle between the axial direction and the point on the Coanda surface, where the skin-friction coefficient, C_f, is locally minimized, becomes almost zero, then returns to higher values (Subhash & Dumas, 2013). For each VR, the separation angles, θ_s, at the upper Coanda surface of the FTV system are tabulated in Table 4 as the points of minimum C_f, which are compared with the results of the gradient-based optimization solution in the next section. As expected, the jet deflection angle increases as VR

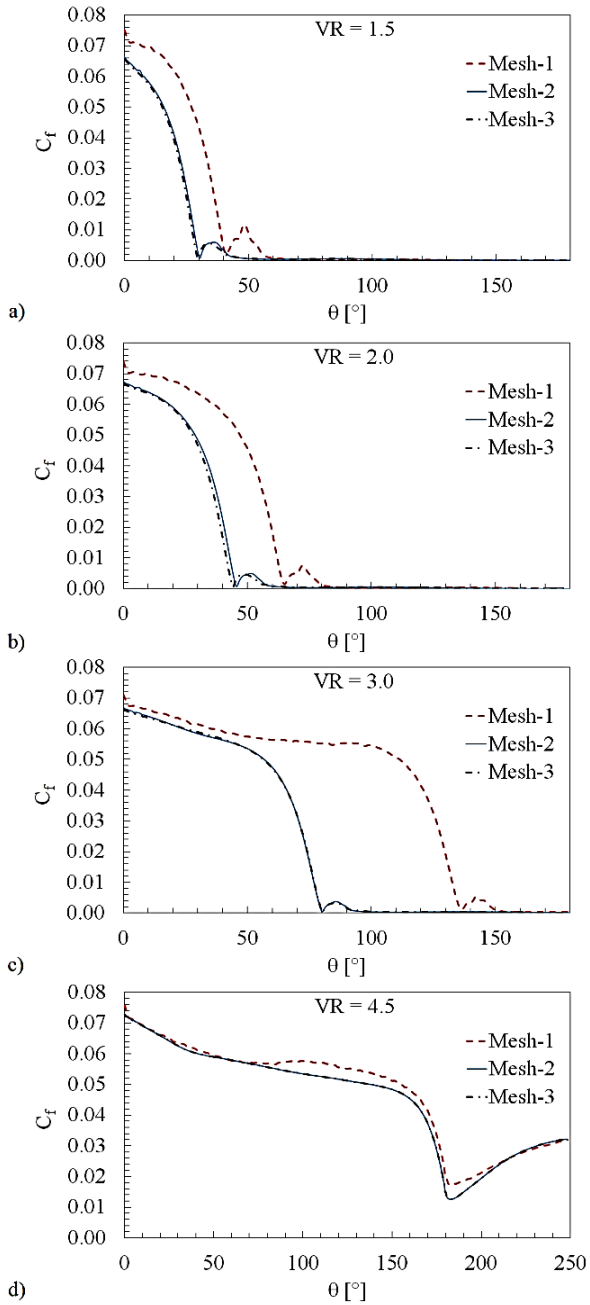

Fig. 8 Comparison of the skin-friction coefficient, C_f, on the upper Coanda surface of FTV system for (a) VR = 1.5; (b) VR = 2.0; (c) VR = 3.0; (d) VR = 4.5

increases, which is shown in Table 4. Other output parameters shown in the table are discussed in the next subsection.

3.3 Representations of Jet Vectoring and Flow Separation

Figure 10 shows the jet deflection differences between VRs = 1.5, 2.0, 3.0, and 4.5. For example, θ_s is 80.00° for VR = 3.0 and close to 182.86° for VR = 4.5. It is clear in Fig. 9 for the value of VR = 4.5 that C_f does not vanish, because the jet flow remains attached to the Coanda surface from 0° to 180° as shown in Fig. 10d. In Fig. 10, the mixing of the co-flow results in a jet directed upward from the throat by the Coanda effect, i.e. the change of the

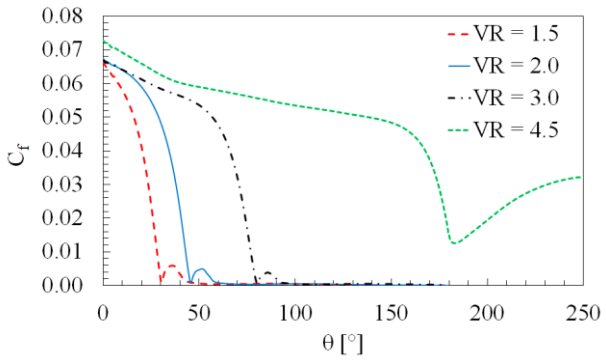

Fig. 9 Variation of C_f on the upper Coanda surface of FTV system for different VRs

flow direction towards the slope of the surface due to the adhesion force exerted on the surface by the fluid itself as a high-velocity fluidic jet passes over a convex surface. Amplifying the VR gradually from 1.5 to 4.5 results in a smoother velocity profile and higher velocity magnitude within the jet stream, which is accomplished through the Coanda effect resulting from the curved surface and the change in pressure in the direction of the flow. Substantial improvement in velocity can be observed in Figs. 13 to 16.

3.4 Gradient-based Optimization Results

In this study, it is intended to delay the separation on the upper Coanda surface of the proposed FTV system for different VRs and thus improve the efficiency of the FTV system. Using the gradient-based optimization module of Ansys Fluent, the shapes of the upper Coanda surface and pintle (recommended locations for the FTV at the start of gradient-based optimization in Ansys Fluent) are optimized to increase the separation angle for each VR studied. The optimization process comprises four steps suggested in ANSYS (2022) manual. First, CFD studies are performed for the mesh-independent computational domain, which is the initially known state of the shape (discussed in the "Mesh Independence Study Results" subsection). Second, the gradient of the observable (in this case, the moment around the upper Coanda surface, $\vec{M}_A$) in the flow direction is calculated and the adjoint solver is performed in parallel with the flow solution. Third, the sensitivity data of the observable is sent back to update and distort the mesh according to the new shapes of the upper Coanda surface and the pintle. Finally, the optimum evolution of the design is reached at the specified threshold or after a maximum number of iterations. An example geometry for the optimized surfaces on the proposed FTV system in Design-4 and the adjoint optimization history are shown in Fig. 11.

The results of the optimization procedure are summarized in Table 5. For all VRs, at the end of the gradient-based optimization, all optimized parameters are significantly higher than the original parameters. The maximum efficiency improvement is reached for the first optimized design, which is optimized with a 17% increase in PP and a 16% increase in η. Correspondingly, thrust vectoring angle, θ_T, and total thrust, T exhibit the best improvement among all designs (17% and 27%,

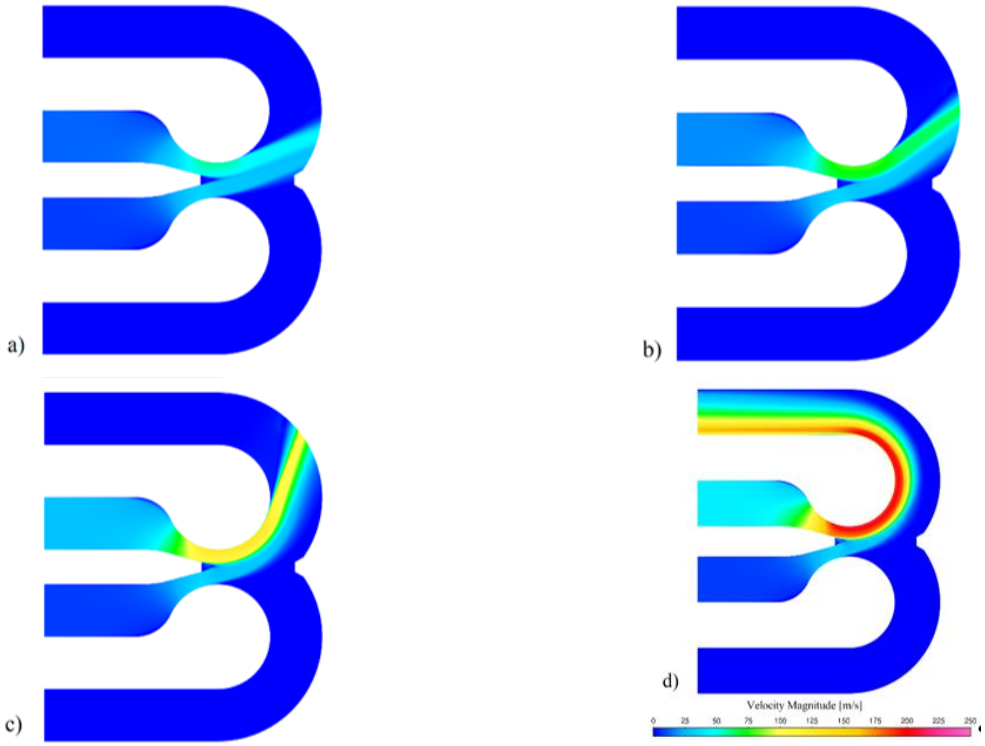

Fig. 10 Differences of jet deflection angles, θ_s, for (a) VR = 1.5; (b) VR = 2.0; (c) VR = 3.0; (d) VR = 4.5

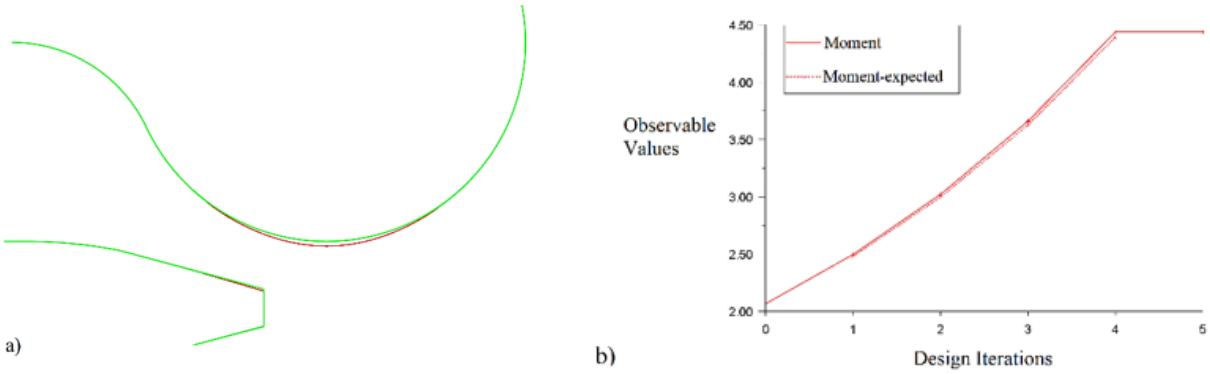

Fig. 11 (a) Optimized surfaces (red lines) compared to original surfaces (green lines) on the proposed FTV system in Design-4; (b) adjoint optimization history of moment around upper Coanda surface, $\vec{M}_A$

Table 5 Parameter space of original design and optimized design results

VR	Input: $\lvert\vec{M}_A\rvert$ (N.m)	Original or optimized configuration	Output: PP	Output: θ_T (°)	Output: η (%)	Output: T (N)	Output: T_y (N)	Output: T_x (N)
1.5	0.025	Original	35.14	21.15	3.99	6.334	3.299	5.395
	0.046	**Optimized (% difference)**	**41.27 (17%)**	**24.83 (17%)**	**4.61 (16%)**	**8.035 (27%)**	**3.836 (16%)**	**7.061 (31%)**
2.0	0.075	Original	54.32	36.43	10.32	10.829	8.536	6.664
	0.211	**Optimized (% difference)**	**61.09 (12%)**	**40.96 (12%)**	**11.26 (9%)**	**12.167 (12%)**	**9.363 (9%)**	**7.771 (17%)**
3.0	0.314	Original	91.13	69.23	31.04	25.689	25.668	-1.043
	0.570	**Optimized (% difference)**	**97.32 (7%)**	**73.94 (7%)**	**33.67 (8%)**	**28.162 (9%)**	**28.006 (9%)**	**-2.957 (183%)**
4.5	1.713	Original	201.27	169.14	12.44	82.685	10.286	-82.042
	4.436	**Optimized (% difference)**	**213.37 (6%)**	**179.70 (6%)**	**12.98 (4%)**	**83.186 (1%)**	**10.798 (5%)**	**-82.482 (1%)**

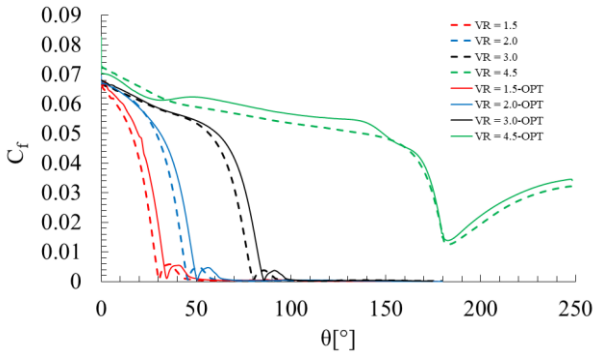

Fig. 12 Variation of C_f on the upper Coanda surfaces of FTV system for different VRs compared to optimized surfaces

Table 6 Comparisons of original and optimized configuration values of jet deflection angle, θ_s for different VR values

	Jet deflection angle, θ_s (°)		
VR	Original	Optimized	Improvement (%)
1.5	31.00	34.37	10.88
2.0	45.50	50.74	11.51
3.0	80.00	85.55	6.94
4.5	182.86	182.87	5.47E-3

respectively). However, the effects of T_x and T_y are not directly related to the efficiency parameters. The effect of the input parameter, $\vec{M}_A$, should be discussed separately as it is the observable parameter and cannot be classified under the same conditions as the parameter space.

Increasing θ_s above 80° leads to a degradation of efficiency (η) independent of the mesh size, while PP, θ_T, and $\vec{M}_A$ still tend to improve. As a result, the most efficient VR is found to be 3.0 when only η is considered. In addition, according to Trancossi's performance parameter, the most efficient VR is found to be 4.5. This issue is investigated after gradient-based optimization studies are presented. After reaching VR = 3.0, it is observed that the negative flow direction also affects T_x values, so thrust vectoring efficiency is expected to increase after this threshold.

The skin-friction coefficient, C_f at the upper Coanda surface also increases after gradient-based optimization for all VRs, as shown in Fig. 12. As indicated in the third column of Table 6, the maximum improvement in θ_s is captured for the second optimized design. However, it is found that the results do not differ too much from the first optimized design.

The differences in jet deflection angles, θ_s, for these VRs and magnified views of velocity vectors near the separation points for the original geometry and the optimized geometry are given in Fig. 13. A close inspection of Fig. 13 reveals that a small increase of 3.37° in θ_s from 31° to 34.37° (10.88% increase) as a result of the optimization leads the velocity vectors slightly towards the Coanda surface, but for VR = 1.5 the change in the direction is not easily captured in the velocity contours. Nevertheless, the change in the flow direction can be more easily followed by examining the velocity

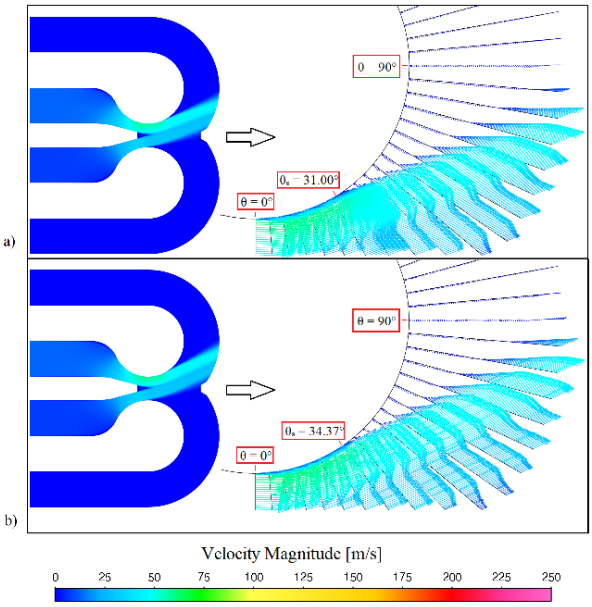

Fig. 13 Differences of separation angle, θ_s, for VR = 1.5 and velocity vectors near the separation points (a) for original geometry compared to (b) for optimized geometry (Design-1)

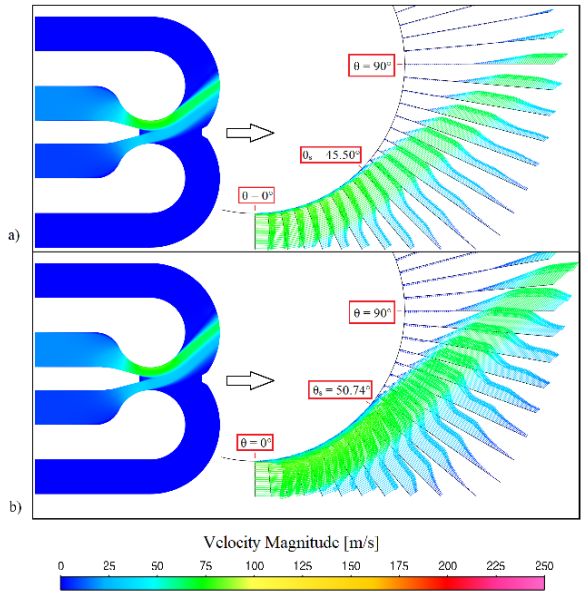

Fig. 14 Differences of separation angle, θ_s, for VR = 2.0 and velocity vectors near the separation points (a) for original geometry compared to (b) for optimized geometry (Design-2)

contours and vectors for VR = 2.0, where there is a large increase of 5.24° in θ_s from 45.50° to 50.74° (11.51% increase) in Fig. 14. Similarly, in Fig. 15, there is a larger increase of 5.55° in θ_s from 80.00° to 80.55° (6.94% increase) for VR = 3.0. In Fig. 16, a minimal 0.01° increase in θ_s (0.00547% increase) is indicated for the optimized geometry for VR = 4.5.

Cross-matching of four optimal design proposals for all VRs examined is tabulated in Table 7, with the maximum results in bold and the runner-ups highlighted in red. The most successful design, that is Design-4, stands out with 15 maxima and 5 runner-ups. The second best

Table 7 Results of optimized parameter space for all optimum design suggestions for all studied VRs

VR	Optimum Design Name	PP	θ_T (°)	η (%)	T (N)	T_y (N)	T_x (N)
1.5	Design-1 (Opt. for VR = 1.5)	**41.27**	**24.83**	**4.61**	**8.035**	**3.836**	7.061
	Design-2 (Opt. for VR = 2.0)	34.85	20.97	3.94	8.022	3.274	**7.324**
	Design-3 (Opt. for VR = 3.0)	34.16	20.55	3.88	6.345	3.224	5.465
	Design-4 (Opt. for VR = 4.5)	40.13	24.15	4.56	6.530	3.792	5.316
2.0	Design-1 (Opt. for VR = 1.5)	59.51	39.91	11.07	**12.199**	9.210	**8.000**
	Design-2 (Opt. for VR = 2.0)	61.09	40.96	11.25	12.167	9.363	7.771
	Design-3 (Opt. for VR = 3.0)	55.73	37.37	10.51	10.920	8.744	6.542
	Design-4 (Opt. for VR = 4.5)	**68.92**	**46.23**	**12.50**	11.528	**10.397**	4.979
3.0	Design-1 (Opt. for VR = 1.5)	91.28	69.36	27.20	22.626	21.292	**7.654**
	Design-2 (Opt. for VR = 2.0)	90.25	68.56	30.77	25.620	25.592	1.202
	Design-3 (Opt. for VR = 3.0)	97.32	73.94	33.67	28.162	28.006	-2.957
	Design-4 (Opt. for VR = 4.5)	**101.84**	**77.43**	**38.12**	**32.017**	**31.713**	-4.402
4.5	Design-1 (Opt. for VR = 1.5)	197.81	166.59	12.84	81.427	10.680	-80.723
	Design-2 (Opt. for VR = 2.0)	200.77	169.08	12.48	80.945	10.381	-80.277
	Design-3 (Opt. for VR = 3.0)	197.81	166.59	12.61	82.262	10.489	-81.590
	Design-4 (Opt. for VR = 4.5)	**213.37**	**179.70**	**12.98**	**83.186**	**10.798**	**-82.482**

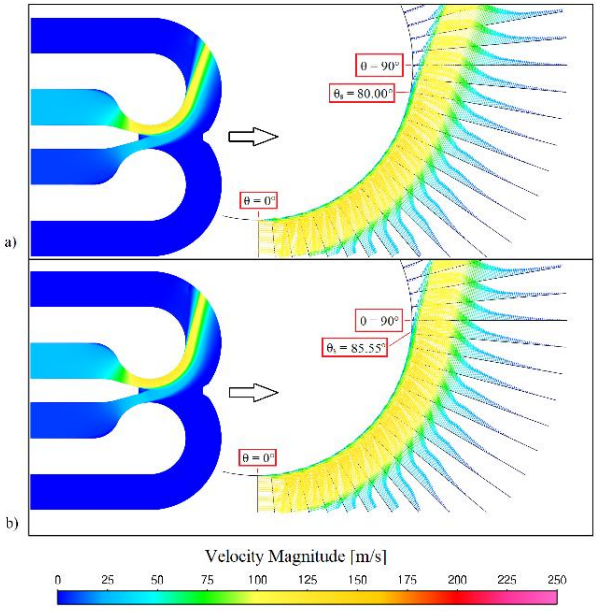

Fig. 15 Differences of separation angle, θ_s, for VR = 3.0 and velocity vectors near the separation points (a) for original geometry compared to (b) for optimized geometry (Design-3)

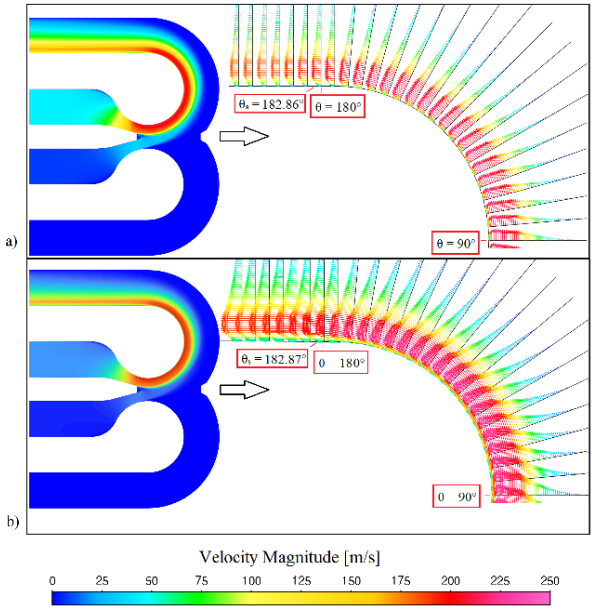

Fig. 16 Differences of separation angle, θ_s, for VR = 4.5 and velocity vectors near the separation points (a) for original geometry compared to (b) for optimized geometry (Design-4)

design is Design-1 with 8 maxima and 3 runner-ups. The least successful design is Design-3 with only 7 runner-ups. Fig. 17 also shows the comparison of C_f variations with θ for the tested designs for each VR. A close inspection of the respective figures shows that Design-1 and Design-4 stand out by delaying the detachment threshold more effectively than Design-2 and Design-3. Between Design-1 and Design-4, the continuity of the C_f data is better and smoother for Design-4.

As a result, the maximum effect of gradient-based optimization is obtained for VR = 2.0 in terms of the percent changes summarized in Table 6. The jet flow (red section) is less dissolved into the flow (green section) in Fig. 16b compared to Fig. 16a, so the jet flow adheres more to the geometry when the geometry is optimized.

The values of jet deflection angle, θ_s, for all tested VRs, are tabulated in Table 8. It is numerically proven that Design-4 is the best choice in terms of maximum separation angle among all designs for VR = 2.0, 3.0, and 4.5 and close to the maximum for VR = 1.5. The analyses show that Design-4 is the most efficient geometry with the best separation delay performance.

4. CONCLUSION

Accurate and exact regulation of aircraft thrust during take-off and landing operations and improved maneuverability are key benefits of FTV systems for the aviation industry. The proposed FTV system is capable of directing thrust in any preferred direction without the need

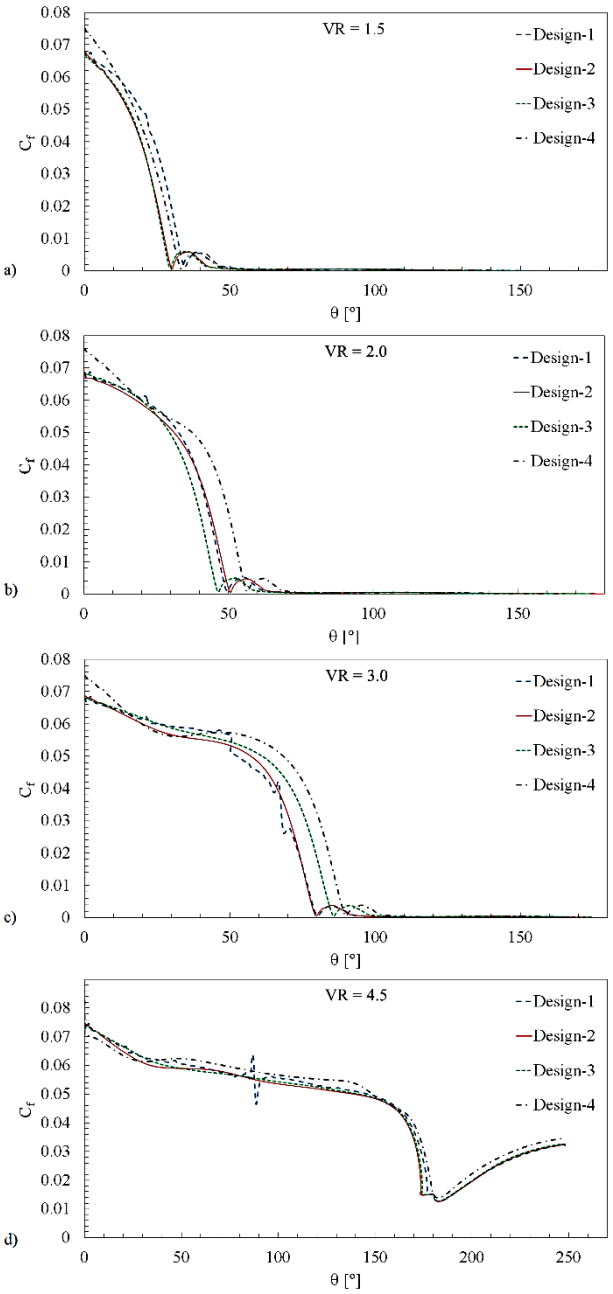

Fig. 17 Variation of C_f on the upper Coanda surfaces of FTV system for (a) VR = 1.5; (b) VR = 2.0; (c) VR = 3.0; (d) VR = 4.5, using the optimized designs

for any movable components, accomplished by utilizing the Coanda effect on the outlet surfaces. This paper numerically examines the FTV system by utilizing CFD and an optimization technique based on gradients of the system components to comprehend the physics of the Coanda effect in FTV systems. It is aimed to determine the optimum parameter space of the FTV system based on the Coanda effect. Gradient-based optimization is employed for nozzle design in order to optimize the parameter space for different VRs by calculating themoment around the upper Coanda surface, which is used to represent the jet deflection angle.

Initially, mesh independence test is performed to determine the optimal mesh for the study. For the final mesh, the first layer height is chosen to be 5×10^{-6} m to meet the criterion of $y^+ < 1$ at boundaries. Using the optimal mesh, four different Coanda surface-pintle pairs were generated for four different VRs. The optimum parameter space values increased in all four configurations. The results show that all output parameters successfully delay separation on the upper Coanda surface. Finally, four optimum design suggestions were tested at various VRs, and the most efficient and proper design was recommended based on output parameters. The outcomes of the study can be summarized as follows:

Table 8 Comparisons of optimized designs in jet deflection angle, θ_s for all VRs

VR	Optimum Design Name	θ_s (°)
1.5	Design-1 (Opt. for VR = 1.5)	34.37
	Design-2 (Opt. for VR = 2.0)	30.76
	Design-3 (Opt. for VR = 3.0)	29.72
	Design-4 (Opt. for VR = 4.5)	33.07
2.0	Design-1 (Opt. for VR = 1.5)	49.45
	Design-2 (Opt. for VR = 2.0)	50.74
	Design-3 (Opt. for VR = 3.0)	46.24
	Design-4 (Opt. for VR = 4.5)	56.39
3.0	Design-1 (Opt. for VR = 1.5)	80.61
	Design-2 (Opt. for VR = 2.0)	79.60
	Design-3 (Opt. for VR = 3.0)	85.55
	Design-4 (Opt. for VR = 4.5)	90.00
4.5	Design-1 (Opt. for VR = 1.5)	182.89
	Design-2 (Opt. for VR = 2.0)	182.86
	Design-3 (Opt. for VR = 3.0)	182.86
	Design-4 (Opt. for VR = 4.5)	182.87

1. Gradual elevation of the VR from 1.5 to 4.5 produces a more uniform velocity profile and a greater velocity magnitude within the jet stream. This is achieved through the Coanda effect and the pressure change in the downstream direction.

2. Upon the conclusion of the gradient-based optimization, all the VRs have substantially increased their optimized parameters compared to the initial values. The maximum efficiency growths are reached for the first optimized design. For all designs, thrust vectoring angle, θ_T, and total thrust, T are the most improved parameters among the other parameters.

3. Increasing θ_s above 80° causes an efficiency degradation (η) independent of the mesh size, while PP, θ_T, and $\vec{M}_A$ increase. As a result, the most efficient VR is found to be 3.0 when only η is considered, despite the fact that the most efficient VR is 4.5 according to Trancossi's performance parameter.

4. After extensive calculations and deliberations concerning the original design, Design-4 is proposed as the most efficient and suitable design with the best separation delay performance based on PP, θ_T, η, T, T_x, T_y, and C_f as the optimized parameter space.

Some future perspectives of the study can be summarized as follows. It is believed that researchers in thrust/jet-propulsion vectoring system development

projects can benefit from presented results for there are no currently available extensive studies in literature that use gradient-based optimization for nozzle design to optimize the parameter space for different velocity ratios to delay separation. Additionally, a subsequent experimental research on the same topic is in progress, which aims to further justify the derived conclusions by validating the numerical results via experimental tests.

ACKNOWLEDGEMENTS

This work is supported by the Scientific Research Projects (BAP) unit of Gaziantep University, Turkey under the grant number of HUBF.GAP.21.02. Computing resources used in this work were provided by the National Center for High Performance Computing of Turkey (UHeM) under grant number 1013062022.

CONFLICT OF INTEREST

No potential conflict of interest was reported by the authors.

AUTHORS CONTRIBUTION

The contribution role of E. Kara includes conceptualization, data curation, formal analysis, funding acquisition, investigation, methodology, project administration, validation, visualization, writing – original draft, and writing – review & editing. The contribution role of D. F. Kurtuluş includes conceptualization, formal analysis, supervision, and writing – review & editing.

REFERENCES

ACHEON. (2015). Final Report. https://cordis.europa.eu/docs/results/309/309041/final1-acheon-final-att.pdf

ANSYS Fluent User's Guide. (2022). http://www.ansys.com

Banazadeh, A., & Saghafi, F. (2017). An investigation of empirical formulation and design optimisation of co-flow fluidic thrust vectoring nozzles. *The Aeronautical Journal*, 121(1236), 213–236. https://doi.org/10.1017/aer.2016.110

Cen, Z., Smith, T., Stewart, P., & Stewart, J. (2015). Integrated flight/thrust vectoring control for jet-powered unmanned aerial vehicles with ACHEON propulsion. *Proceedings of the Institution of Mechanical Engineers, Part G: Journal of Aerospace Engineering*, 229(6), 1057–1075. https://doi.org/10.1177/0954410014544179

Das, S. S., Páscoa, J. C., Trancossi, M., & Dumas, A. (2016). Computational fluid dynamic study on a novel propulsive system: ACHEON and its integration with an unmanned aerial vehicle (UAV). *Journal of Aerospace Engineering*, 29(1), 04015015. https://doi.org/10.1061/(ASCE)AS.1943-5525.0000498

El Halal, Y., Marques, C. H., Rocha, L. A., Isoldi, L. A., Lemos, R. D. L., Fragassa, C., & Dos Santos, E. D. (2019). Numerical study of turbulent air and water flows in a nozzle based on the Coanda effect. *Journal of Marine Science and Engineering*, 7(2), 21, 1–13. https://doi.org/10.3390/jmse7020021

Jain, S., Roy, S., Gupta, D., Kumar, V., & Kumar, N. (2015). Study on fluidic thrust vectoring techniques for application in V/STOL aircrafts. *SAE Technical Paper*, No. 2015–01–2423. https://doi.org/10.4271/2015-01-2423

Juvet, P. (1994). Control of high Reynolds number round jets. (Publication No. 9414588). [Doctoral dissertation, Stanford University]. ProQuest Dissertations and Theses Global.

Kara, E., & Erpulat, H. (2021). Experimental investigation and numerical verification of Coanda effect on curved surfaces using co-flow thrust vectoring. *International Advanced Researches and Engineering Journal* 5 (1), 72–78. https://doi.org/10.35860/iarej.758397

Menter, F. R., Sechner, R., & Matyushenko, A. (2019). Best practice: generalized k-ω two-equation turbulence model in ANSYS CFD (GEKO). https://fluidcodes.com/wpcontent/uploads/2020/06/geko-tp-1.pdf

Menter, F. R., Sechner, R., & Matyushenko, A. (2021). Best practice: RANS turbulence modelling in ANSYS CFD. https://www.ansys.com/content/dam/amp/2022/march/quickrequest/Best%20Practice%20RANS%20Turbulence%20Modeling%20in%20Ansys%20CFD.pdf

Newman, B. G. (1961). The deflexion of plane jet by adjacent boundaries coanda effect. In C. Maykel & M. A. Bray (Eds.), *Boundary layer and flow control* Vol. 1 (pp. 232–264). Pergamon Press. https://www.sciencedirect.com/book/9781483213231/boundary-layer-and-flow-control

Panneer, M., & Thiyagu, R. (2020). Design and analysis of Coanda effect nozzle with two independent streams. *International Journal of Ambient Energy*, 41(8), 851–860. https://doi.org/10.1080/01430750.2018.1480524

Roache, P. J. (1994). Perspective: a method for uniform reporting of grid refinement studies. *ASME Journal of Fluids Engineering*, 116(3), 405–13. https://doi.org/10.1115/1.2910291

Sidiropoulos, V., & Vlachopoulos, J. (2000). An investigation of Venturi and Coanda effects in blown film cooling. *International Polymer Processing*, 15(1), 40–45. https://doi.org/10.3139/217.1575

Springer, A. M. (2008, January 7-10). *50 Years of NASA Aeronautics Achievements* [Conference session]. 46. AIAA Aerospace Sciences Meeting and Exhibit, Reno, Nevada, United States. https://doi.org/10.2514/6.2008-859

Subhash, M., & Dumas, A. (2013). Computational study of Coanda adhesion over curved surface. *SAE*

International Journal of Aerospace, 6(1), 260. https://doi.org/10.4271/2013-01-2302

Trancossi, M., & Dumas, A. (2011). ACHEON: Aerial coanda high efficiency orienting-jet nozzle. *SAE Technical Paper*, No. 2011–01–2737. https://doi.org/10.4271/2011-01-2737

Trancossi, M., Dumas, A., Das, S. S., & Pascoa, J. (2014). Design methods of Coanda effect nozzle with two streams. *Incas Bulletin*, 6(1), 83–95. https://doi.org/10.13111/2066-8201.2014.6.1.8

Trancossi, M., Dumas, A., Giuliani, I., & Baffigi I. (2011). *Nozzle capable of deviating a synthetic jet in adynamic and controllable manner with nomoving mechanical parts and a control system thereof.* Patent No. RE2011A000049, Italy. https://patentscope.wipo.int/search/en/detail.jsf?docId=IT231131498&_cid=P22-LI8YNL-59892-1

Trancossi, M., Madonia, M., Dumas, A., Angeli, D., C. Bingham, Das, S. S., Grimaccia, F., Marques, J. P., Porreca, E., Smith, T., Stewart, P., Subhash, M., Sunol, A., & Vucinic, D. (2016a). A new aircraft architecture based on the ACHEON Coanda effect nozzle: flight model and energy evaluation. *European Transport Research Review*, 8(2), 1–21. https://doi.org/10.1007/s12544-016-0198-4

Trancossi, M., Stewart, J., Maharshi, S., & Angeli, D. (2016b). Mathematical model of a constructal Coanda effect nozzle. *Journal of Applied Fluid Mechanics*, 9(6), 2813–2822. https://doi.org/10.29252/jafm.09.06.23508

Warsop, C., Crowther, W. & Forster, M. (2019, January 7-11). *NATO AVT-239 Task Group: Supercritical Coanda based circulation control and fluidic thrust vectoring* [Conference session]. AIAA Scitech 2019, San Diego, California, United States. https://doi.org/10.2514/6.2019-0044

Wu, K., Zhang, G., Kim, T. H., & Kim, H. D. (2020). Numerical parametric study on three-dimensional rectangular counter-flow thrust vectoring control. *Proceedings of the Institution of Mechanical Engineers, Part G: Journal of Aerospace Engineering*, 234(16), 2221–2247. https://doi.org/10.1177/0954410020925602

Yahaghi, A. (2011). *Computational study of fluidic thrust vectoring using shock vector and separation control.* [Master's thesis, San Jose State University]. California, United States. https://www-old.sjsu.edu/ae/docs/project-thesis/Amir%20Yahaghi-converted.pdf